Measurement of the Second-Order Polarizability of Silver Nanoparticles With Reference-Free Hyper-Rayleigh Scattering for Entangled Photon Pair Interaction

Ariel Ashkenazy, Racheli Ron, Tchiya Zar, Hannah Aharon, Adi Salomon, Dror Fixler, and Eliahu Cohen

***Abstract*—Two-photon interactions of entangled-photon pairs with metallic nanoparticles (NPs) can be enhanced by localized surface-plasmon resonance. Recently, we have described how the properties of this quantum light-matter interaction can be deduced from classical second-harmonic generation measurements performed using a reference-free hyper-Rayleigh scattering method. Herein, we report the results of such classical-light characterization measurements. We obtain a large hyperpolarizability for the NPs, present the dependence of the hyperpolarizability on the NPs' spectral features, and show a dipolar emission pattern for the second-harmonic signal. Our results can be used to optimize entangled-photon pair interactions with metallic NPs to enable first ever detection of this process. Moreover, these results suggest that NPs may be used as source for ultra-broadband entangled-photon pairs through nonphase-matched spontaneous parametric down-conversion.**

***Index Terms*—Entangled photons, hyper-Rayleigh scattering, nanoparticles, second-harmonic generation.**

I. Introduction

ENERGY-TIME entangled-photon pairs (EPP), commonly generated through spontaneous parametric down-conversion (SPDC) in nonlinear crystals, possess strong spectral and temporal correlations simultaneously [1]. These correlations can then be exploited, for example, in advanced quantum spectroscopy schemes [2], [3]. Moreover, at low photon flux regime, where on average only a single pair occupies each temporal mode, the quantum correlations of EPPs result in a two-photon interaction rate which is linear in the EPPs flux, as opposed to the quadratic dependence on incident flux observed with classical light [4]. Thus, it was suggested that EPPs may be used to achieve strong two-photon interactions in ultra-low photon flux regime [5], *e.g.*, for two-photon sensing of photosensitive molecules. These promising features have sparked a lot of interest in two-photon EPPs interaction (EPPI) [6]–[10]. However, recent studies have shown that, due to the weakness of two-photon interactions and the low EPPs flux in the single-pair regime, EPPI with matter is expected to be around the noise limit of common systems [11]–[13]. This limitation gives rise to a need for improving the employed techniques for EPPI and optimizing the properties of the interaction medium. For telecommunication wavelengths, dielectric (AlGaAs) nanoantennas were shown to achieve high second-harmonic generation (SHG) conversion efficiency, which translates to high EPPI or SPDC capabilities [14], [15]. However, for visible-light wavelengths, the search for enhanced EPPI rate is still an open question.

One suggested way to achieve stronger EPPI is to make use of metallic nanoparticles (NPs), whose localized surface-plasmon resonance (LSPR) can enhance linear and nonlinear interactions [16]–[20]. Ashkenazy et al. have described how the expected enhancement of EPPI (specifically, SHG) with NPs can be deduced from classical-light SHG measurements performed in a novel reference-free hyper-Rayleigh scattering (RFHRS) method [21], [22]. They have shown that, for an aqueous solution of a mixture of triangular and spherical silver NPs (SNPs), LSPR results in NPs having hyperpolarizability that is three orders-of-magnitude larger than best organic molecules. Still, the EPPI rate with NPs is expected to be rather low and further optimization of the process, as well as a deeper understanding of it, are needed.

To that end, we report here classical-light characterization measurements performed using the RFHRS method on samples of silver nanocubes (SNCs) and nanoplates of triangular shape

Manuscript received 3 April 2022; revised 28 June 2022; accepted 27 July 2022. Date of publication 3 August 2022; date of current version 15 August 2022. The work of Ariel Ashkenazy was supported in part by the Planning and Budgeting Committee of Israel's Council of Higher Education Fellowship for Excellent Ph.D. Students in Quantum Science and Technology and in part by the Bar-Ilan University President's Scholarship Program for Outstanding Ph.D. students. The work of Eliahu Cohen was supported in part by Foundational Questions Institute and Fetzer Franklin Fund under Grant FQXi-RFP-CPW-2006, in part by the donor-advised fund of Silicon Valley Community Foundation, in part by the Israeli Innovation Authority under Grants 70002 (Quantum Illumination) and 73795 (Quantum Communication Consortium), in part by the Pazy foundation, in part by the Israeli Ministry of Science and Technology, in part by Elta Systems, and in part by the Quantum Science and Technology Program of the Israeli Council of Higher Education *(Corresponding author: Eliahu Cohen.)*

Ariel Ashkenazy, Dror Fixler, and Eliahu Cohen are with the Faculty of Engineering and the Institute of Nanotechnology and Advanced Materials, Bar Ilan University, Ramat Gan 5290002, Israel (e-mail: ariel.ashkenazy@biu.ac.il; dror.fixler@biu.ac.il; eliahu.cohen@biu.ac.il).

Racheli Ron, Tchiya Zar, Hannah Aharon, and Adi Salomon are with the Chemistry Department and the Institute of Nanotechnology and Advanced Materials, Bar Ilan University, Ramat Gan 5290002, Israel (e-mail: rachel.ron@biu.ac.il; tchiya.zar@biu.ac.il; hannah.aharon@biu.ac.il; adi.salomon@biu.ac.il).

This article has supplementary downloadable material available at https://doi.org/10.1109/JPHOT.2022.3196243, provided by the authors.

Digital Object Identifier 10.1109/JPHOT.2022.3196243

This work is licensed under a Creative Commons Attribution 4.0 License. For more information, see https://creativecommons.org/licenses/by/4.0/

(SNTs). These SNPs were embedded in polyvinyl-alcohol (PVA), making it the first report of RFHRS measurements on NPs embedded in a homogenous media and not in a solution. Moreover, unlike previous experimental setups [21], [22] in which the transmitted second-harmonic (SH) signal was measured, in our implementation the SH signal was measured in reflection.

In the experiments we were able to record significant SHG in the SNPs. The obtained hyperpolarizabilities were of the same order-of-magnitude as previous reports in the literature (in which traditional hyper-Rayleigh scattering method was used), showing the validity and robustness of the RFHRS method in various implementations. Additionally, in this set of experiments, we characterized the SHG in SNPs in terms of the dependence on excitation wavelength. The results, analyzed based on the theory behind RFHRS, showed a clear dependence of the hyperpolarizability on the SNPs' spectral features and an excellent agreement with theoretical models, in contrast with previous report in the literature. Finally, polarization-dependent measurements of the SHG in SNPs were performed, showing a dipolar emission pattern.

The paper is organized as follows. In Materials and Methods we discuss the essential theoretical aspects of SHG in NPs and the RFHRS method, describe the SNCs and SNTs samples used in our experiments, and present the optical setup. Then, in the Results and Analysis section, we report the outcomes of our characterization measurements and extract the relevant properties from these outcomes. We then present a Discussion of the obtained results and draw some Conclusions regarding EPPI with NPs. The discussion outlines the main contributions of the work that include a novel RFHRS method for optimizing, for the first time, various metallic nanoparticles for SHG and possibly also for SPDC.

II. Materials and Methods

A. SHG in NPs and the RFHRS Method

Within the electric-dipole approximation, the second-order susceptibility of centrosymmetric crystals, such as gold and silver, is zero [23], [24]. Nevertheless, reports of SHG in plasmonic nanostructures can be found in the literature, both for colloidal NPs [25] and for structured arrays [26]. For small NPs, these nonlinear signals can be explained as originating from the surface of the nanostructure, where the centrosymmetry is broken. In the far field, this surface contribution is possible only for particles of noncentrosymmetric shape. Thus, using NPs of noncentrosymmetric shape for SHG should be advantageous. In practice, though, no particles of perfect centrosymmetric shape exist, so some surface SHG is always present [27]. The SHG in NPs can be enhanced by tuning the LSPR near either the fundamental frequency (FF) or the SH (or even both, see, for example, [28]), but the former might lead to increased absorption of the high intensity pump, damaging the sample [29]. Moreover, the interaction is not restricted by phase-matching constraints thanks to the negligible propagation length relative to optical wavelengths [29].

Description of SHG in NPs is usually done in terms of their hyperpolarizability, β, which relates the induced SH dipole moment, $p_{2\omega}$, to the electric field, $p_{2\omega} = \beta E^2$, in accordance with the B-convention [30]. Hyperpolarizability is usually measured in electrostatic units, where $1[esu] = 3.7133 \times 10^{-21}[C^3 m^3 J^{-2}]$. The hyperpolarizability of colloidal NPs is traditionally obtained using the hyper-Rayleigh scattering method in which incoherent SH signal ($I_{2\omega}$) is recorded *vs.* incident intensity (I_ω). These are related by [25]:

$$I_{2\omega} = G \left\langle C_{sol}\beta_{sol}^2 + C_{NP}\beta_{NP}^2 \right\rangle I_\omega^2 A, \tag{1}$$

with C_{sol} and C_{NP} being the concentration of solvent molecules and NPs, respectively, and A representing the transmission of the SH signal through the system. The triangular brackets stand for averaging over all possible orientations. The G-factor (having units of $[s \cdot F^{-3} \cdot m^{-1}]$) is a geometrical factor accounting for the specific details of the optical setup. In this method, in order to extract β_{NP}, the G-factor must be known. To that end, additional reference measurements are required [31].

In [22], Ashkenazy et al. have proposed a different approach, a RFHRS method, in which the NPs are modeled as dipoles oscillating at the SH frequency, and the G-factor (for setups in which the SH signal is collected in reflection or transmission) is approximated as:

$$G \approx \frac{2V\omega^4}{\pi^2 \varepsilon_0^3 c^5 r^2}, \tag{2}$$

where V is the volume of interaction, ε_0 is the permittivity of the vacuum, c is the speed of light in vacuum, and r is the distance from the sample to the collecting lens. With this method, no additional reference measurements are needed. To estimate the hyperpolarizability, one plots the SH signal as a function of the square of the incident intensity and apply a linear fit. The slope of this fit, is then used to extract the hyperpolarizability through (1).

EPPI rate is usually expressed in terms of total SH photon counts rate ($S_{SH}[s^{-1}]$), the quantum yield of the SHG process (η), the EPPI cross-section ($\sigma_e[\text{cm}^2]$) and the incident photon flux ($\Phi_{in}[s^{-1}\text{cm}^{-2}]$). In the single-pair regime, due to the strong quantum correlation between the photons of each pair, S_{SH} is linear in the incident flux and given by [32]:

$$S_{SH} = \eta \sigma_e \Phi_{in}. \tag{3}$$

Based on the G-factor approximation, the EPPI cross-section can be related to the NPs' hyperpolarizability through [22]:

$$\eta\sigma_e = \frac{4\hbar\omega^5 \left\langle \beta_{NP}^2 \right\rangle}{3\pi\varepsilon_0^3 c^5 A_e T_e} = \frac{\eta\sigma_c}{2A_e T_e}, \tag{4}$$

with A_e (T_e) being the entanglement area (time), *i.e.*, the area (time) within which the two photons of the pair are created in the crystal. σ_c is the classical-light two-photon interaction cross-section of the NPs, measured in GM units ($1[GM] = 10^{-50}[\text{cm}^4 \cdot s]$).

Although the RFHRS method was originally derived for NPs' solutions, it is valid also for our samples which are PVA-embedded (as described below), since the equations that describe the interaction are the same for both cases, see [33].

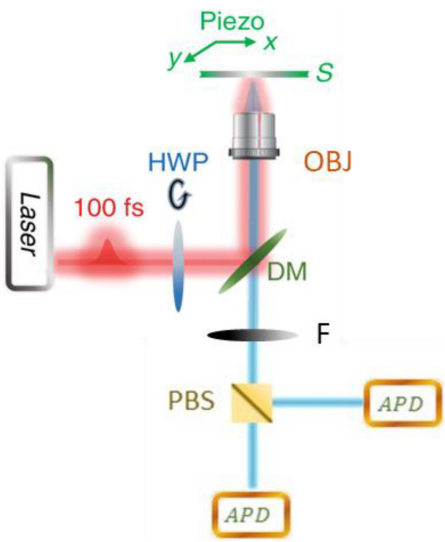

Fig. 1. Schematic diagram of optical setup used for RFHRS measurements. HWP – half-wavelength plate, DM – dichroic mirror, OBJ – objective lens, S – sample, F – bandpass filters, PBS – polarizing beam-splitter, APD – avalanche photodiode.

B. Optical Setup

The optical setup (Fig. 1) consisted of a pulsed Ti:Sapphire laser (Spectra-Physics Mai-Tai HP) with repetition rate $\nu =$ 80[MHz] and pulse duration $\tau_p = 100[fs]$, tunable in the range of 690–1080[nm]. The polarization of the incident light was chosen by a rotating half-wavelength plate. Using an $\times 50$ objective lens ($N.A. = 0.5$) the light was then focused on the sample, which was mounted on a piezo stage (Piezosystem Jena). The diameter of the beam incident on the sample was $D_{beam} \approx 2.2[\mu\text{m}]$. The reflected SH signal was collected by the same lens. The FF light was filtered out by a dichroic mirror (Chroma) and a set of bandpass filters (Semrock). The signal then passed through a polarizing beam splitter towards two avalanche photodiodes (PerkinElmer), thus recording the SH intensity in two perpendicular polarizations. The results were obtained in terms of total SH photo-counts per second (CPS). The background noise of the system was about $100[CPS]$ ($\sim 0.02[fW]$). The transmittance of the system components at the SH wavelength was calculated to be $T_{system} \approx 0.1$.

To minimize the effect of thermal processes on our measurements, we shifted the location of the focal spot on the sample each time that a parameter (*e.g.*, incident power or wavelength) was changed. Then, the reported CPS values were obtained by averaging over the detectors' readings in the first few integration cycles only (*i.e.*, prior to signal degradation). The standard deviations of these CPS readings are given as error bars in the figures.

C. Samples

PVP-stabilized solutions of SNCs and SNTs, were purchased from nanoComposix, Inc. (San Diego, CA, USA. The data presented in Table I, Figs. 2, 3 and Fig. S.1, were provided by them). The full description of both solutions is given in Table I.

TABLE I
PARAMETERS OF SNCS AND SNTS SOLUTIONS

Solution	Diameter $[nm]$	Original concentration $[\times 10^{11}\ \#/mL]$	Solvent	pH
SNCs	74 ± 7	2.6	Ethanol	8.9
SNTs	31.5 ± 8.1	62.9	Aqueous $5mM$ sodium borate	8.9

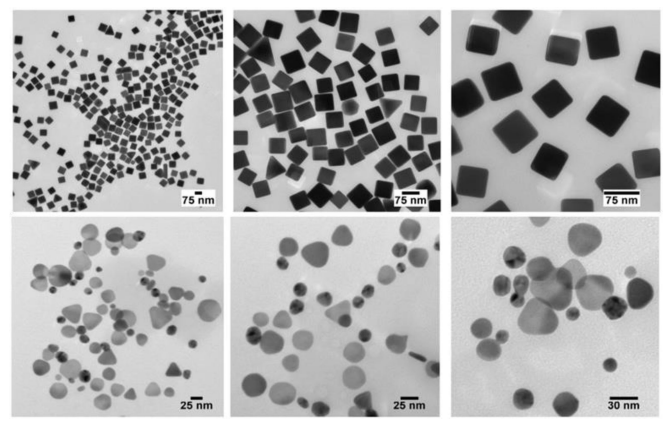

Fig. 2. TEM images of SNCs (top) and SNT (bottom) solutions.

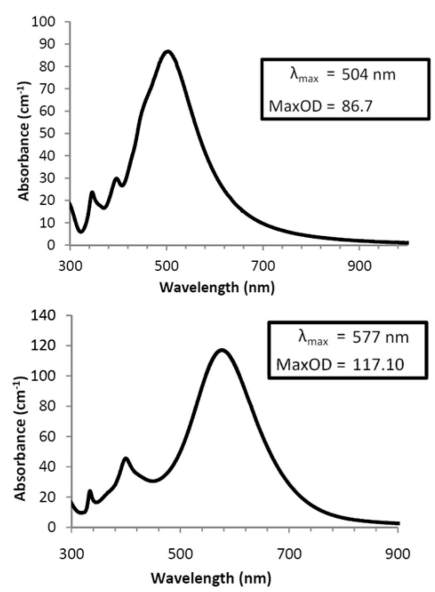

Fig. 3. Absorption spectra of SNCs (top) and SNTs (bottom).

The diameter of the NPs is defined as the cube's diagonal (for SNCs) or the triangle's height (for SNTs).

TEM images of the solutions are presented in Fig. 2. The solutions' spectra, including the LSPR wavelength and maximal optical density (OD), are shown in Fig. 3. Histograms of the size distributions of the solutions are given in Supplement 1 (Fig. S.1).

The original Ag mass concentration of both solutions was about $\sim 1[\text{mg/mL}]$. For our experiments, we have diluted the solutions (each solution in its respective solvent) $\times 10$ and $\times 100$ (for SNTs only), *i.e.*, down to Ag mass concentration of $0.1[\text{mg/mL}]$ and $0.01[\text{mg/mL}]$, respectively. These diluted solutions were then mixed with an aqueous solution of PVA ($40[\text{mg/mL}]$, $89{,}000 - 98{,}000[\text{MW}]$, purchased from Sigma-Aldrich). Later, $100[\mu\text{L}]$ of the PVA-SNPs solution were drop-casted on pre-treated glass-slides. The glass-slides were left to dry in a vacuum chamber, forming our PVA-embedded samples. We denote the samples with a superscript identifying the Ag mass concentration in the sample, *e.g.*, $\text{SNTs}^{0.1}$ for PVA-embedded SNTs with $0.1[\text{mg/mL}]$ Ag mass concentration. Even after the dilution, the number of NPs in the interaction volume is still large (≥ 40 for all samples), and so the directional averaging over the ensemble (assumed in (1)) is justified.

The width of the resulting PVA-embedded SNCs (SNTs) samples was $l_{SNC} = 385[\mu\text{m}]$ ($l_{SNT} = 278[\mu\text{m}]$), measured by scanning the focal plane of a microscope across the width of the samples.

The glass pre-treatment included bath-sonication of each glass-slide in 1% aqueous solution of Hellmanex for $25[\text{min}]$ under mild heating ($35°C$), followed by thorough washing with ddH_2O and drying under N_2 (99.999%) flow.

III. Results and Analysis

We performed RFHRS measurements where the SH power scattered from the samples ($\text{SNCs}^{0.1}$, $\text{SNTs}^{0.1}$ and $\text{SNTs}^{0.01}$) was measured as a function of the square of the incident power. We used excitation wavelength of $\lambda = 980[\text{nm}]$ for the SNCs, and $\lambda = 940[\text{nm}]$ for the SNTs, such that the SH wavelength is near the main LSPR peak of the SNCs and near a minimum point in the SNTs' spectrum. Fig. 4 shows the results of these measurements – SH power ($P_{2\omega}$) as a function of the incident FF power squared (P_ω^2). Due to the low NPs concentration, the signal for $\text{SNTs}^{0.01}$ is weak, and so the standard deviation of the results is larger, especially for high incident power, where thermal effects are more dominant.

A linear fit of the results showed good agreement ($R^2 \geq 0.96$) and yielded the following slopes:

$$M_{SNC^{0.1}} = 3.9 \times 10^{-10}\left[W^{-1}\right]$$
$$M_{SNT^{0.1}} = 1.7 \times 10^{-10}\left[W^{-1}\right]$$
$$M_{SNT^{0.01}} = 1.37 \times 10^{-11}\left[W^{-1}\right]. \quad (5)$$

These slopes are inserted into (1) to extract the samples' hyperpolarizabilities, as described in Supplement 1. The obtained hyperpolarizabilities, as well as the samples' classical-light two-photon interaction cross-section ($\eta\sigma_c$) (using (4)), are presented in Table II. The obtained hyperpolarizabilities are within an estimated uncertainty of 16% (14%) for the $\text{SNC}^{0.1}$ ($\text{SNT}^{0.1}$) samples, and 27% for the $\text{SNT}^{0.01}$ sample.

From the obtained hyperpolarizabilities we can estimate the EPPI cross-section of the NPs, using (4). For entangled photons generated through SPDC in nonlinear crystals, the entanglement area is roughly the EPP spot area [34]. We take a typical value of

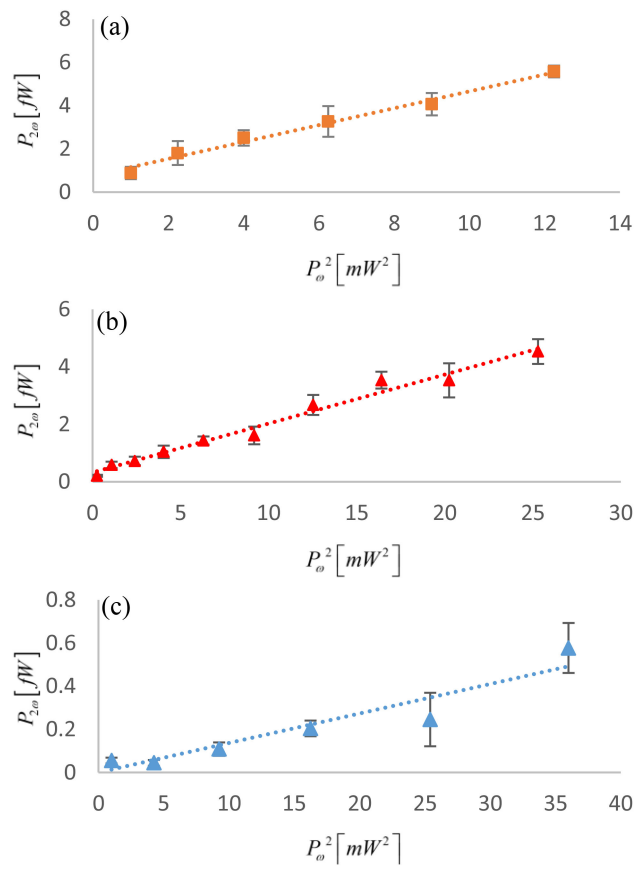

Fig. 4. Power of SH generated in $\text{SNCs}^{0.1}$ (a) and in $\text{SNTs}^{0.1}$ (b) and $\text{SNTs}^{0.01}$ (c) as a function of the square of the incident power. Slope of the linear fit of the results is used to extract the samples' hyperpolarizability.

TABLE II
Hyperpolarizability and Classical-Light Two-Photon Interaction Cross-Section Obtained for PVA-Embedded Samples Using the RFHRS Method

Sample	$\langle\beta_{NP}\rangle[\times 10^{-25} esu]$	$\eta\sigma_c[GM]$
$\text{SNC}^{0.1}$	16.45	520.96
$\text{SNT}^{0.1}$	1.89	8.5
$\text{SNT}^{0.01}$	1.52	5.51

$A_e = 50[\mu\text{m}^2]$. Reported values for the entanglement time are commonly in the range of tens to hundreds of femto-seconds (see, for example, [35]), and we take a typical value of $T_e = 50[\text{fs}]$. With these values we get:

$$\eta\sigma_e^{SNC^{0.1}} = 10.42 \times 10^{-29}\left[\text{cm}^2\right]$$
$$\eta\sigma_e^{SNT^{0.1}} = 0.17 \times 10^{-29}\left[\text{cm}^2\right]$$
$$\eta\sigma_e^{SNT^{0.01}} = 0.11 \times 10^{-29}\left[\text{cm}^2\right]. \quad (6)$$

These results fit excellently the theoretical bound derived by Parzuchowski et al. [11]. According to their derivation, EPPI cross-section of such magnitude will yield an EPPI signal that is almost imperceptible. This indicates, once more, the importance

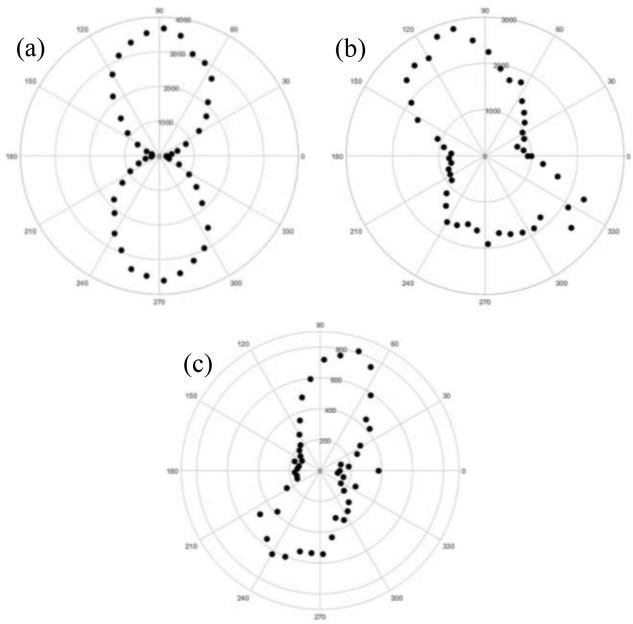

Fig. 5. Radiation patterns of a calibration silver film (a), SNCs (b) and SNTs (c) all exhibiting a dipolar pattern.

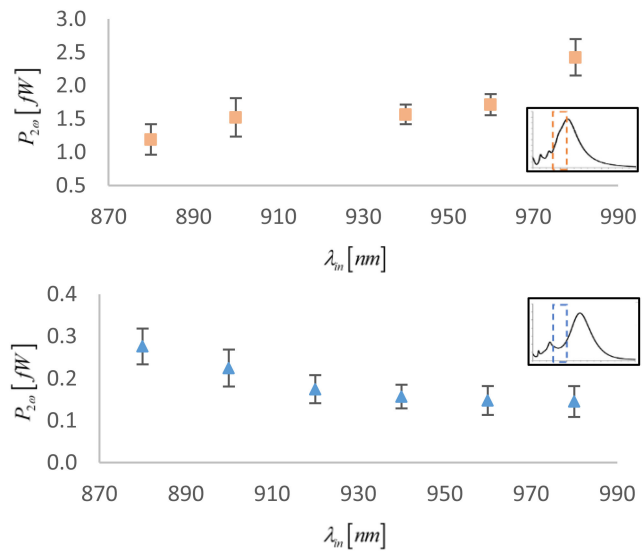

Fig. 6. SH power generated in SNCs (top) and SNTs (bottom) as a function of incident wavelength. Inserts show the spectra of the nanoparticles in the range of the SH of the excitation wavelengths.

of characterization of EPPI with NPs, as described herein, to allow for optimization of this process.

We also performed measurements of the SH photon CPS in one polarization channel as a function of the angle of polarization of the incident laser. These measurements were performed on SNCs$^{0.1}$ and SNTs$^{0.01}$, using an excitation wavelength of $940[nm]$. The system was calibrated using a silver film known to exhibit a dipolar emission pattern. The calibration and measurement results are all shown in Fig. 5.

Lastly, we measured the dependence of the SH power on the wavelength of the incident laser, λ_{in}, while keeping the laser power constant. Due to the filters and detectors in the setup, the valid range for the excitation laser was $880 - 980[nm]$. We performed these measurements on SNCs$^{0.1}$ with $P_\omega = 1.5[mW]$ and SNTs$^{0.01}$ with $P_\omega = 4[mW]$, and obtained the results presented in Fig. 6.

VI. Discussion

Following the results of the RFHRS measurements (Table II), it can be seen that the hyperpolarizability of SNCs provides further support to the credibility of the RFHRS method, as it is in excellent agreement with the value reported by Russier-Antoine et al. in [36] ($16.6 \times 10^{-25}[esu]$ for SNCs with edge length of 48[nm]) measured using the traditional hyper-Rayleigh scattering method. Moreover, the current results were obtained using a new configuration for the RFHRS measurements, different from the one used in [22], with the SNPs being embedded in PVA and the SH signal collected in reflection. Thus, the results reported herein show not only the accuracy of the RFHRS method but also its applicability to any optical setup configuration, a testimony to this method's simplicity and versatility.

The SH intensity for the low-concentration SNT$^{0.01}$ sample was about 10 times weaker relative to that of the high-concentration SNT$^{0.1}$ sample, *i.e.*, a linear dependence of the SH intensity on NPs concentration. This result is in line with (1), and shows that indeed the process is incoherent hyper-Rayleigh scattering, since for a coherent process a quadratic dependence of the SH intensity on NPs concentration is expected [37]. As for the hyperpolarizability, since it is a property of the individual NPs it therefore should be the same regardless of the sample's concentration. Indeed, the obtained values of $\langle \beta_{NP} \rangle$ for both our SNTs samples, having different NPs concentration, are of the same order-of-magnitude, as expected, and the small difference in these $\langle \beta_{NP} \rangle$ values is within the estimated uncertainties of the results.

The hyperpolarizability obtained for the SNCs is rather similar to the values previously reported in [22] for aqueous solutions of a mixture of silver nanospheres and nanotriangles. However, we must take into account the fact that our SNCs were much larger in size (with a diameter of about 74[nm] as compared to a diameter of 25[nm] for the NPs solutions used in [22]), and so a true comparison must be performed on a per-atom basis. In this aspect, the hyperpolarizability-per-atom of the SNCs is appreciably smaller than that of the samples used in [22], by a factor of more than 50, which is roughly the ratio of the volume of our SNCs to that of spherical NPs with a diameter of 25[nm] (for the triangular shaped NPs the ratio will be even bigger). We thus conclude that triangular shaped NPs, exhibiting much higher hyperpolarizability-per-atom than SNCs, are more suitable for SHG (and EPPI), presumably due to their noncentrosymmetric shape (as opposed to cubes [36]).

However, our SNTs samples showed rather weak SHG capabilities, with an order-of-magnitude smaller hyperpolarizability relative to the samples from [22]. This is because our SNTs samples had an LSPR peak (577[nm]) that was not tuned near

the SH wavelength (440 – 490[nm]). The obvious conclusion is that, while choosing the appropriate geometry for the NPs is important, properly tuning the LSPR of the NPs around the SH wavelength is crucial for efficient EPPI with NPs.

The polarization measurement results, presented in Fig. 5(b) and (c), show a clear dipolar emission pattern, as can be seen by comparison to the dipolar emission pattern of the calibration silver film (a), with the small orientation deviations of the NPs' polar plots attributed to misalignment error, as the experiments were conducted on different days. Since the G-factor approximation is based on the description of the NPs as oscillating dipoles, these results support the theoretical derivation of the G-factor and validate its use for RFHRS measurements. This is also in perfect agreement with the polarization plots reported in [36] and [38].

Finally, we analyze the dependence of the SH signal on the excitation wavelength, shown in Fig. 6. The results show the SH signal to (almost monotonically) increase with increasing excitation wavelength for the SNCs, and an opposite behavior for the SNTs, with no resemblance to the NPs' spectral shape. Reports of such measurement of the SHG in NPs (rather than nanoarrays) as a function of incident wavelength are not so common, but a behavior similar to our results had been reported before by Yashunin et al. [39] who concluded that, since none of the features of the NPs' extinction spectrum (including their LSPR peak) is presented in the results, the common theoretical models of hyper-Rayleigh scattering must be incorrect. However, based on our G-factor approximation, we propose an explanation for the results. We note that the SH signal depends on the excitation wavelength not only through the NPs' hyperpolarizability, but also through the G-factor and the SH transmission term, A, as can be seen in (1). Thus, one has to find the dependence of the hyperpolarizability itself on the excitation wavelength, and there the spectral features should be apparent. Since RFHRS method gives us the dependence of the G-factor on the excitation wavelength (through (2)), and since the extinction spectra of the samples are known (Fig. 3), we can use the results of Fig. 6, together with (1), to extract a crude estimation of the SNPs hyperpolarizability *vs.* excitation wavelength, see Supplement 1. The results of this procedure are shown in Fig. 7.

We see that, for SNCs, the hyperpolarizability indeed increases monotonically with increasing excitation wavelength. This is in line with the SNCs extinction spectrum, Fig. 3, that is also increasing monotonically in the range of $440 - 490[nm]$ (which is the range of the SH signal in our measurements). For the SNTs, however, the graph of the hyperpolarizability *vs.* excitation wavelength approaches a minimum point near $940[nm]$ (corresponding to SH wavelength of $470[nm]$) and then starts increasing. This again is in line with the SNTs extinction spectrum, which exhibits a minimum point in the range of $440 - 490[nm]$.

Thus, using the G-factor approximation, we are able to explain the dependence of the SH signal on the excitation wavelength, in contrast with previous reports in literature, and the results match perfectly the theoretical models of hyper-Rayleigh scattering, and show once again the important effect of LSPR on SHG in NPs.

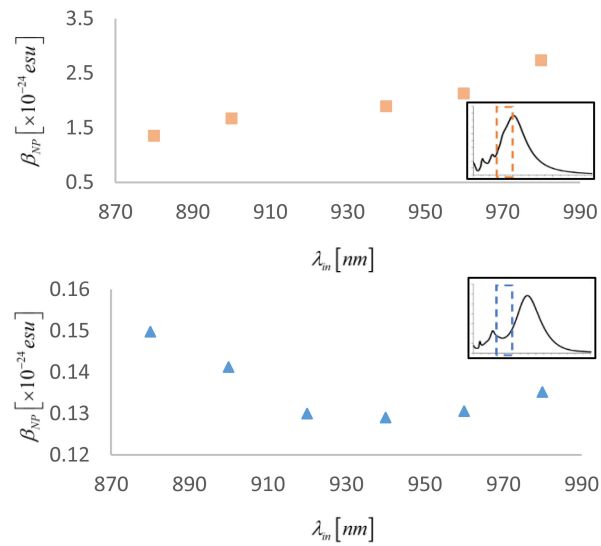

Fig. 7. Hyperpolarizability of SNCs (top) and SNTs (bottom) as a function of incident wavelength showing the characteristics of the NPs' absorption spectra. Inserts show the spectra of the nanoparticles in the range of the SH of the excitation wavelengths.

V. Conclusion

In this paper we use the RFHRS method, with which the results of classical-light SHG can be related to the expected properties of EPPI with NPs, for characterization of this interaction to allow its optimization. The method is implemented in a novel way, measuring the reflected classical-light SH signal from silver nanocubes and nanotriangles embedded in PVA. The hyperpolarizabilities obtained in the experiments show excellent agreement with previous reports, performed in the common hyper-Rayleigh scattering method (with reference measurements), testifying for the validity of the RFHRS method and its applicability for different optical setup configurations. This method can simplify tremendously the procedure of hyperpolarizability measurements in the future, as it requires no additional reference measurements.

The EPPI cross-sections of the samples were estimated based on the classical-light RFHRS results. The obtained σ_e fits perfectly the theoretical bound reported in literature. The results indicate that indeed EPPI with NPs is expected to be extremely weak, emphasizing the importance of our characterization measurements reported herein, and that this interaction might be observable only if proper optimization of the experimental concept is performed. For example, since the SH signal increases linearly with NPs concentration, it may be advantageous to have the NPs in solution, where the concentration is much higher than that of PVA-embedded samples.

Comparing the results of the hyperpolarizabilities of our SNCs and SNTs samples we reach the conclusion that optimal EPPI requires both choosing NPs of noncentrosymmetrical shape *and* tuning the LSPR of the NPs at the SH wavelength.

This conclusion is also supported by the wavelength-dependent measurements. Previously reported results of such measurements were declared inexplicable. We, however, have offered a solution to this problem and showed that the

hyperpolarizability indeed expresses the spectral features of the NPs, as predicted by the theoretical models. Thus, we deduce that fine tuning of the LSPR wavelength is essential for the enhancement of NPs hyperpolarizability and with that their expected EPPI rate.

Finally, polarization measurements were conducted, exhibiting dipolar emission pattern for both SNCs and SNTs samples. This result validates that the main contribution for SHG in our NPs is of an electric dipole nature, in agreement with the results reported in [40], and is probably originating from symmetry breaking at the surface of the NPs.

With the results reported herein, experiments aiming to detect EPPI in NPs can be optimized to maximize the interaction rate and the detection efficiency. This holds the promise for experimental observation of EPPI with matter, a crucial element for applications such as quantum spectroscopy with capabilities beyond classical limits [2], [3]. Furthermore, strong EPPI with NPs indicates strong SPDC capabilities, as this is the time reversed process of EPPI. Since the propagation length through the NPs is negligible relative to optical wavelengths, no phase-matching is required, as opposed to the commonly used nonlinear crystals and thus such NPs' based SPDC have the potential of generating ultra-broadband energy-time entangled photons [41], with multiple applications to quantum sensing and cryptography [42].

References

[1] S. Lerch and A. Stefanov, "Observing the transition from quantum to classical energy correlations with photon pairs," *Commun. Phys.,* vol. 1, no. 26, pp. 1–6, 2018, doi: 10.1038/s42005-018-0027-2.

[2] K. E. Dorfman, F. Schlawin, and S. Mukamel, "Nonlinear optical signals and spectroscopy with quantum light," *Rev. Mod. Phys.,* vol. 88, no. 4, 2016, Art. no. 045008, doi: 10.1103/RevModPhys.88.045008.

[3] F. Schlawin, "Entangled photon spectroscopy," *J. Phys. B: At. Mol. Opt. Phys.,* vol. 50, no. 20, 2017, Art. no. 203001, doi: 10.1088/1361-6455/aa8a7a.

[4] B. Dayan, "Theory of two-photon interactions with broadband down-converted light and entangled photons," *Phys. Rev. A,* vol. 76, no. 4, 2007, Art. no. 043813, doi: 10.1103/PhysRevA.76.043813.

[5] D.-I. Lee and T. Goodson, "Entangled photon absorption in an organic porphyrin dendrimer," *J. Phys. Chem. B,* vol. 110, pp. 25582–25585, 2006, doi: 10.1021/jp066767g.

[6] E. G. Carnio, A. Buchleitner, and F. Schlawin, "How to optimize the absorption of two entangled photons," *SciPost Phys. Core,* vol. 4, no. 28, 2021, Art. no. 028, doi: 10.21468/SciPostPhysCore.4.4.028.

[7] S. Lerch and A. Stefanov, "Experimental requirements for entangled two-photon spectroscopy," *J. Chem. Phys.,* vol. 155, no. 6, 2021, Art. no. 064201, doi: 10.1063/5.0050657.

[8] B. Li and H. F. Hofmann, "Energy-time entanglement and intermediate-state dynamics in two-photon absorption," *Phys. Rev. A,* vol. 104, no. 2, 2021, Art. no. 022434, doi: 10.1103/PhysRevA.104.022434.

[9] H. Oka, "Highly-efficient entangled two-photon absorption with the assistance of plasmon nanoantenna," *J. Phys. B: At. Mol. Opt. Phys.,* vol. 48, no. 11, 2015, Art. no. 115503, doi: 10.1088/0953-4075/48/11/115503.

[10] J. P. Villabona-Monsalve, R. K. Burdick, and T. Goodson, "Measurements of entangled two-photon absorption in organic molecules with CW-pumped Type-I spontaneous parametric down-conversion," *J. Phys. Chem. C,* vol. 124, pp. 24526–24532, 2020, doi: 10.1021/acs.jpcc.0c08678.

[11] K. M. Parzuchowski et al., "Setting bounds on entangled two-photon absorption cross sections in common fluorophores," *Phys. Rev. Appl.,* vol. 15, no. 4, 2021, Art. no. 044012, doi: 10.1103/PhysRevApplied.15.044012.

[12] M. G. Raymer, T. Landes, M. Allgaier, S. Merkouche, B. J. Smith, and A. H. Marcus, "How large is the quantum enhancement of two-photon absorption by time-frequency entanglement of photon pairs?," *Optica,* vol. 8, no. 5, pp. 757–758, 2021, doi: 10.1364/OPTICA.426674.

[13] M. G. Raymer, T. Landes, and A. H. Marcus, "Entangled two-photon absorption by atoms and molecules: A quantum optics tutorial," *J. Chem. Phys.,* vol. 155, no. 8, 2021, Art. no. 081501, doi: 10.1063/5.0049338.

[14] G. Marino et al., "Spontaneous photon-pair generation from a dielectric nanoantenna," *Optica,* vol. 6, no. 11, pp. 1416–1422, 2019, doi: 10.1364/OPTICA.6.001416.

[15] V. F. Gili et al., "Monolithic AlGaAs second-harmonic nanoantennas," *Opt. Exp.,* vol. 24, no. 14, pp. 15965–15971, 2016, doi: 10.1364/OE.24.015965.

[16] R. Ankri et al., "Gold nanorods based air scanning electron microscopy and diffusion reflection imaging for mapping tumor margins in squamous cell carcinoma," *ACS Nano,* vol. 10, no. 2, pp. 2349–2356, 2016, doi: 10.1021/acsnano.5b07114.

[17] M. Beiderman et al., "Gold nanorod-based bio-barcode sensor array for enzymatic detection in biomedical applications," *ACS Appl. Nano Mater.,* vol. 3, no. 8, pp. 8414–8423, 2020, doi: 10.1021/acsanm.0c01819.

[18] K. Imura, T. Nagahara, and H. Okamoto, "Near-field two-photon-induced photoluminescence from single gold nanorods and imaging of plasmon modes," *J. Phys. Chem. B,* vol. 109, pp. 13214–13220, 2005, doi: 10.1021/jp051631o.

[19] S. A. Maier, *Plasmonics: Fundamentals and Applications*, 1st ed., Berlin, Germany: Springer, 2007.

[20] S. Sudri et al., "Diffusion reflection method for early detection of oral squamous cell carcinoma specifically targeted by circulating gold-nanorods bio-conjugated to anti-epidermal growth factor receptor," *Int. J. Nanomed.,* vol. 16, pp. 2237–2246, 2021, doi: 10.2147/IJN.S300125.

[21] A. Ashkenazy, A. Stefanov, and D. Fixler, "Enhanced entangled-photon-pair interaction with metallic nanoparticles," in *Proc. SPIE*, 2019, vol. 10891, Art. no. 108910V, doi: 10.1117/12.2509949.

[22] A. Ashkenazy, K. Wang, M. Unternährer, D. Fixler, and A. Stefanov, "Estimation of the rate of entangled-photon-pair interaction with metallic nanoparticles based on classical-light second-harmonic generation measurements," *J. Phys. B: At. Mol. Opt. Phys.,* vol. 52, no. 14, 2019, Art. no. 145401, doi: 10.1088/1361-6455/ab0e5e.

[23] R. W. Boyd, *Nonlinear Optics*, 3rd ed., Cambridge, MA, USA: Academic, 2008.

[24] J. Butet, P. F. Brevet, and O. J. Martin, "Optical second harmonic generation in plasmonic nanostructures: From fundamental principles to advanced applications," *ACS Nano,* vol. 9, no. 11, pp. 10545–10562, 2015, doi: 10.1021/acsnano.5b04373.

[25] F. W. Vance, B. I. Lemon, and J. T. Hupp, "Enormous hyper rayleigh scattering from nanocrystalline gold particle suspension," *J. Phys. Chem. B,* vol. 102, no. 50, pp. 10091–10093, 1998, doi: 10.1021/jp984044u.

[26] A. Salomon, M. Zielinski, R. Kolkowski, J. Zyss, and Y. Prior, "Size and shape resonances in second harmonic generation from silver nanocavities," *J. Phys. Chem. C,* vol. 117, no. 43, pp. 22377–22382, 2013, doi: 10.1021/jp403010q.

[27] M. G. Papadopoulos, A. J. Sadlej, and J. Leszczynski, *Non-Linear Optical Properties of Matter* (Challenges and Advances in Computational Chemistry). Berlin, Germany: Springer, 2006.

[28] M. Celebrano et al., "Mode matching in multiresonant plasmonic nanoantennas for enhanced second harmonic generation," *Nat. Nanotechnol.,* vol. 10, no. 5, pp. 412–417, 2015, doi: 10.1038/nnano.2015.69.

[29] G. P. Wiederrecht, *Handbook of Nanoscale Optics and Electronics*. Amsterdam, The Netherlands: Elsevier, 2010.

[30] H. Reis, "Problems in the comparison of theoretical and experimental hyperpolarizabilities revisited," *J. Chem. Phys.,* vol. 125, no. 1, 2006, Art. no. 014506, doi: 10.1063/1.2211611.

[31] E. Hendrickx, K. Clays, and A. Persoons, "Hyper-Rayleigh scattering in isotropic solution," *Acc. Chem. Res.,* vol. 31, pp. 675–683, 1998, doi: 10.1021/ar960233o.

[32] J. Gea-Banacloche, "Two-photon absorption of nonclassical light," *Phys. Rev. Lett.,* vol. 62, no. 14, pp. 1603–1606, 1989, doi: 10.1103/PhysRevLett.62.1603.

[33] J. Butet et al., "Optical second harmonic generation of single metallic nanoparticles embedded in a homogeneous medium," *Nano Lett.,* vol. 10, no. 5, pp. 1717–1721, 2010, doi: 10.1021/nl1000949.

[34] T. Landes, M. G. Raymer, M. Allgaier, S. Merkouche, B. J. Smith, and A. H. Marcus, "Quantifying the enhancement of two-photon absorption due to spectral-temporal entanglement," *Opt. Exp.,* vol. 29, no. 13, pp. 20022–20033, 2021, doi: 10.1364/OE.422544.

[35] C. Okoth, A. Cavanna, T. Santiago-Cruz, and M. V. Chekhova, "Microscale generation of entangled photons without momentum conservation," *Phys. Rev. Lett.,* vol. 123, no. 26, 2019, Art. no. 263602, doi: 10.1103/PhysRevLett.123.263602.

[36] I. Russier-Antoine et al., "Second harmonic scattering from silver nanocubes," *J. Phys. Chem. C,* vol. 122, no. 30, pp. 17447–17455, 2018, doi: 10.1021/acs.jpcc.8b04299.

[37] K. B. Eisenthal, "Second harmonic spectroscopy of aqueous Nano- and Microparticle interfaces," *Chem. Rev.,* vol. 106, pp. 1462–1477, 2006, doi: 10.1021/cr0403685.

[38] A. K. Singh, D. Senapati, A. Neely, G. Kolawole, C. Hawker, and P. C. Ray, "Nonlinear optical properties of triangular silver nanomaterials," *Chem. Phys. Lett.,* vol. 481, pp. 94–98, 2009, doi: 10.1016/j.cplett.2009.09.045.

[39] D. A. Yashunin, A. I. Korytin, A. I. Smirnov, and A. N. Stepanov, "Second harmonic generation and two-photon luminescence from colloidal gold nanoparticles," *J. Phys. D: Appl. Phys.,* vol. 49, no. 10, 2016, Art. no. 105107, doi: 10.1088/0022-3727/49/10/105107.

[40] J. Nappa, G. Revillod, I. Russier-Antoine, E. Benichou, C. Jonin, and P. F. Brevet, "Electric dipole origin of the second harmonic generation of small metallic particles," *Phys. Rev. B,* vol. 71, no. 16, 2005, Art. no. 165407, doi: 10.1103/PhysRevB.71.165407.

[41] A. Ashkenazy, E. Cohen, and D. Fixler, "Characterization of second-harmonic generation in silver nanoparticles for spontaneous parametric down-conversion," in *Proc. SPIE*, 2022, vol. 12016, Art. no. 1201610, doi: 10.1117/12.2618308.

[42] L. Bello, Y. Michael, M. Rosenbluh, E. Cohen, and A. Pe'er, "Broadband complex two-mode quadratures for quantum optics," *Opt. Exp.,* vol. 29, no. 25, pp. 41282–41302, 2021, doi: 10.1364/OE.432054.